ULTRAFINEGRAINED MATERIALS

Evolution of strength and structure during SPD processing of Ti–45Nb alloys: experiments and simulations

**B. Sulkowski · A. Panigrahi · K. Ozaltin ·
M. Lewandowska · B. Mikułowski ·
M. Zehetbauer**

Abstract A β-phase Ti–45Nb alloy was processed by several severe plastic deformation (SPD) methods as high-pressure torsion, cold rolling and folding, and hydrostatic extrusion to enhance its strength by achieving an ultrafine grained structure without affecting the Young's modulus being close to that of bone material. Mechanical properties during processing were monitored by direct torque and Vickers hardness measurements, while the micro-/nano-structural evolution was investigated by transmission electron microscopy and X-ray line profile analysis. Simulations of both mechanical and micro-/nano-structural data were performed on the basis of the SPD work-hardening model by Zehetbauer. The simulations not only found a good agreement with the deformation-specific evolution of strength and density of individual dislocations but also well reflected mesoscopic structural quantities such as the sizes of cell/grain interiors and walls without introducing additional fitting parameters.

B. Sulkowski (✉) · B. Mikułowski
Department of Material Science and Non-Ferrous Metals Engineering, Faculty of Non-Ferrous Metals, AGH-University of Science and Technology, Mickiewicza Av. 30, 30-059 Kraków, Poland
e-mail: sul5@agh.edu.pl

B. Sulkowski · A. Panigrahi · K. Ozaltin · M. Zehetbauer
Research Group Physics of Nanostructured Materials, Faculty of Physics, University of Vienna, Boltzmanngasse 5, 1090 Wien, Austria
e-mail: michael.zehetbauer@univie.ac.at

K. Ozaltin · M. Lewandowska
Faculty of Materials Science and Engineering, Warsaw University of Technology, Woloska 141, 02-507 Warsaw, Poland

Introduction

In recent years, TiNb based alloys are getting more attention in biomedical research areas because of the unique combination of their properties such as high specific strength, good corrosion resistance and excellent biocompatibility compared to other traditional alloys [1–3]. The alloys used for implants should have Young's moduli close to those of human bones (around 30 GPa) as this condition minimizes the stress shielding effect [4]. In binary Ti–Nb system, the Young's modulus shows a dependence on Nb content and exhibits two local minima, at about 15 and 42.5 wt% Nb, respectively. The single β-phase alloy Ti–45 wt% Nb lies close to the second minimum showing a Young's modulus of 65 GPa [5]. However, the mechanical strength is also much lower [6, 7] than that of other conventional biomedical materials such as Ti–6Al–4V, Ti–6Al–7Nb, Ti–5Al–2.5Fe, etc. On the other hand, it seems possible to increase the mechanical properties of metallic materials significantly by applying methods of severe plastic deformation (SPD) [8, 9], without increasing the Young's modulus [10–13]. Such methods, e.g. cold rolling and folding (CR&F), high-pressure torsion (HPT) or hydrostatic extrusion (HE), are very effective in grain refinement [8]; by applying a high deformation strain, an ultrafine or even nanoscaled structure can be achieved, which results in a marked increase of strength often paired with a considerable plastic deformability [8, 9].

In this investigation, the biomedical alloy Ti–45 wt% Nb was subjected to CR&F, HPT and HE to produce ultrafined or nanostructured bulk material with very high mechanical properties, that is high strength, good plasticity and low Young's modulus. Besides, several mechanical test methods (for the results on Young's modulus, see Ref. [14]) such as transmission electron microscopy (TEM)

have been applied to study the strain-dependent evolution of grain/cell interior and grain/cell size, whereas those of X-ray line profile analyses (XPA) were carried out for obtaining the dislocation density, as well as the coherently scattering domain size (also called 'crystallite size' in the literature). As this latter quantity indicates the smallest size of defect-free regular crystalline area, in largely strained materials it has been repeatedly identified with the area size of the accumulated edge dislocations near the grain/cell boundaries [15–17]. Among other quantities, this edge area size will serve as a useful parameter in the current study in comparing data from experiments with those from simulations. The latter were done using the dislocation-based constitutive large strain work-hardening model by Zehetbauer [18–20]. In several previous publications [8, 15, 16, 21], it has been shown that the model is capable of predicting the strain-dependent evolution of the strength and also the structural features of material such as the dislocation density, the cell/cell wall size, the misorientation angle and the concentration of strain-induced vacancies of SPD-processed materials as the function of external hydrostatic pressure [15, 16, 22].

Methodology

Experiments

The initial material used in this study was a hot-extruded bar of Ti–45Nb alloy. Its chemical composition is listed in Table 1.

The samples for *CR&F processing* were cut from the bar of 42-mm diameter and 10-mm thickness. The CR&F process consisted of several steps of intermediate rolling and folding at room temperature. Steps with (i) no folds, (ii) twofolds and (iii) fourfolds pertained to true strains of 1.5, 3.0 and 4.8, respectively.

The samples for *HPT processing* were disc-shaped with 8-mm diameter and 0.8-mm thickness. The discs were cut by spark erosion machine from an extruded initial bar in a way that the normal direction (ND) of discs was parallel to the radial direction of the initially extruded bar. The HPT experiments were carried out at room temperature at 4 GPa hydrostatic pressure with 0.5, 1, 5 and 10 turns. Additionally, the in situ torque was measured during HPT

processing. The σ–ε (true stress–true strain) curve of the HPT deformation curve is obtained from in situ torque/torsion angle data using the following relations and the Von Mises factor $\sqrt{3}$:

$$\sigma = \sqrt{3}\frac{3Q}{2\pi R^2}, \tag{1}$$

$$\varepsilon = \frac{R\phi}{d\sqrt{3}}, \tag{2}$$

where Q is the measured torque, R is the effective radius of the sample, ϕ is the torsion angle and t is the thickness of the sample.

Concerning *HE processing*, rod-shaped specimens with a diameter of $d_0 = 30$ mm were prepared from the initial material parallel to the extrusion direction, and were subjected to HE in a multi-step process of six passes, by reducing the diameter after each pass. The true strain ε was determined by the relation $\varepsilon = 2\ln(d_f/d_i)$, where d_i and d_f denote the diameter before and after a particular pass. After six passes of HE, the final diameter of each rod was 5 mm with a total accumulated true strain of 3.5.

After each intermediate step of deformation during CR&F, HPT and HE processing, the *Vickers hardness* of the samples was measured. The hardness measurements were carried out using a Vickers micro-hardness tester PAAR MHT 4, and indentations were achieved by a force of 1.96 N and a dwell time of 10 s, on the rolling plane and on the shear plane normal of CR&F and HPT processed samples, respectively. For each value, an average of 10 measurements was taken. All the experimental work-hardening curves were obtained or at least checked by Vickers hardness data. Those of CR&F and HE were done after each pass, respectively (see Table 2). The relation $\sigma = \text{HV}/2.63$ was found by the best fit of Vickers hardness data of HPT-processed sample to the in situ σ–ε true stress–true strain curves obtained from the torque/torsion angle data reported before.

TEM has been carried out by a JEOL M 1200 instrument. The X-ray diffraction profiles of the processed samples were measured at the beamline P07–HEMS at the Synchrotron PETRA 3 HASYLAB Hamburg, Germany, operating at 50 keV ($\lambda = 0.0248$ nm).

The Convolution Multiple Whole Profile (CMWP) fitting procedure was used to determine both the dislocation density and the 'crystallite size'. The CMWP procedure has been described in detail in Refs. [23, 24].

Table 1 Chemical composition of hot-extruded Ti–Nb45 (wt%)

Nb	Fe	Cr	Mn	Mg	Si	K	Na	O	N	Ti
44.94	<0.03	<0.01	<0.01	<0.01	<0.1	<0.01	<0.01	0.095	0.007	bal.

Table 2 Input parameters used for simulations by Zehetbauer's model

Parameter	Notation	Value	Comments
Taylor factor			Taylor factors were calculated from experimental textures in the frame of Taylor model (see 'Methodology' section)
	$\langle M_{CR\&F} \rangle$	2.76	Rolling and folding
	$\langle M_{HPT} \rangle$	2.05	High-pressure torsion
	$\langle M_{HE} \rangle$	2.83	Hydro-extrusion
Fraction factor	$f_1^{CR\&F}$	0.92	Values optimized during simulations considering the enhanced pressures 4 GPa (HPT processing), 1 GPa (HE) and 0.1 MPa (CR&F)
	f_1^{HPT}	0.80	
	f_1^{HE}	0.92	
Dislocation interaction parameters	$\alpha_1^{CR\&F}$	0.31	Values derived from fits of dislocation density
	$\alpha_2^{CR\&F}$	0.36	
	α_1^{HPT}	0.25	
	α_2^{HPT}	0.39	
	α_1^{HE}	0.30	
	α_2^{HE}	0.37	
Vacancy migration enthalpy	δH_m (eV)	0.53	Refs. [27, 28]

Simulations

Description of the Zehetbauer's model

The Zehetbauer's model [15, 16, 18–21] is a composite model, where screw and edge dislocations do not interact with each other because of different strain fields around the cores of dislocations. Thus, they are arranged in separate regions of cell interiors (areas of screw dislocations) and cell walls (areas of edge dislocations). The macroscopic hardening results from a weighted sum of contribution of hardening in cell interiors and cell walls, and can be represented as

$$\frac{\delta\tau}{\delta\gamma} = f_1 \frac{\delta\tau_1}{\delta\gamma_1} + f_2 \frac{\delta\tau_2}{\delta\gamma_2}, \qquad (3)$$

where the 'weights' f_1 and f_2 are the structural fractions of cell/grain interiors and cell walls, respectively; $f_2 = 1 - f_1$. Equation (3) allows to treat work hardening of cell interiors and cell walls separately, according to Eqs. (4) and (5):

$$\frac{\delta\tau_1}{\delta\gamma_1} = C_1 - C_3\tau_1, \qquad (4)$$

$$\frac{\delta\tau_2}{\delta\gamma_2} = C_2 - C_4[\tau_2 - \tau_2(0)]\tau_2^5, \qquad (5)$$

where $C_1, \ldots, C_4$ are constants describing particular processes during SPD processing of the material and are

connected with distinct physical parameters. C_1 and C_2 describe the storage of screw and edge dislocations, respectively, following the expression (6):

$$C_i = \frac{\alpha_i\mu}{2\beta_i}, \quad i = 1, 2, \qquad (6)$$

where μ is shear modulus, $\alpha_i \in \langle 0.3, 1 \rangle$, $\alpha_1 < \alpha_2$ are dislocation interaction parameters, and $\beta_i \in \langle 10, 300 \rangle$ denote the storage rates of specific dislocations with densities ρ_i ($i = 1, 2$ for screws and edges, respectively) relative to their mean free path L_i, in terms of dislocation distance $L_i = 1/\sqrt{\rho_i}$. C_3 describes the annihilation of screw dislocations through the cross-slip mechanism according to Eq. (7):

$$C_3 = \frac{1}{\dot{\gamma}}\omega_d e^{\frac{-\delta G}{kT}}, \qquad (7)$$

where $\dot{\gamma}$ is the strain rate, ω_d is the Debye frequency, δG represents the enthalpy of screw dislocation annihilation, k is Boltzmann constant and T is the absolute temperature. The last parameter, C_4, describes the annihilation of edge dislocations through climb processes, with the aid of deformation-induced vacancies (8):

$$C_4 = \frac{c_v}{[\tau_2 - \tau_2(0)]\frac{\dot{\gamma}kT\alpha_2^4 b^2 \mu^3 \pi(1-\nu)}{\sqrt{2}\ \Omega D_{c,0}}\exp\left(\frac{\delta H_m + p\Omega}{kT}\right)}, \qquad (8)$$

where c_v is the concentration of vacancies, ν is Poisson's ratio, Ω is the atomic volume, $D_{c,0}$ means the core diffusion coefficient, δH_m stands for the vacancy migration enthalpy and p represents the hydrostatic pressure applied during the SPD processing.

Concerning the microstructural quantities, the model firstly provides the dislocation interaction parameters α_i from fits to experimentally measured dislocation densities, according to

$$\rho(\gamma) = \frac{1}{(\mu b)^2}\left(\frac{f_1\tau_1(\gamma)}{\alpha_1} + \frac{f_2\tau_2(\gamma)}{\alpha_2}\right). \qquad (9)$$

Secondly, the grain/cell size L_1 (area of screw dislocations) and cell wall size L_2 (area of edge dislocations) are directly derived from the stress/strain relationships and the α_i/β_i parameters, as

$$L_1 = \frac{\alpha_1\beta_1\mu b}{\tau(\gamma)}, \quad L_2 = \frac{L_1}{f_1} - L_1 \qquad (10)$$

with μ as the shear modulus and b as the Burgers vector.

The misorientation angle θ can be calculated from the expression:

$$\theta = 2k \arcsin\frac{bL_2\rho_2}{2}, \qquad (11)$$

where ρ_2 is the density of sessile dislocations in cell walls (edge areas, with size L_2) and k is a scaling factor [16].

Calculations of resolved shear stress/resolved shear strain data

For application of Zehetbauer's model, datapairs of resolved shear stress–resolved shear strain (τ–γ) must be provided. These τ–γ datapairs can be calculated from stress–strain curves σ–ε by the Taylor factor $\langle M \rangle$ according to the relations: $\tau = \sigma/\langle M \rangle$ and $\gamma = \langle M \rangle \varepsilon$.

The Taylor model [25, 26] was used to determine the Taylor factors for the samples processed by every SPD method used ($\langle M_{\text{CR\&F}} \rangle$, $\langle M_{\text{HPT}} \rangle$ and $\langle M_{\text{HE}} \rangle$). In the Taylor model it is assumed that all the grains experience the same strain. The average volume-weighted Taylor factor $\langle M \rangle$ for the aggregate can be calculated from the equation:

$$\langle M \rangle = \frac{\sum\limits_{i}^{N} M(g_i)}{N}, \qquad (12)$$

where N is a number of crystalline in the aggregate and M is the Taylor factor for the particular crystallite as function of its orientation g_i. The orientations g_i of the crystallite can be obtained from the experimentally measured textures. The measuring procedure and the texture results will be published elsewhere [14]. The Taylor factor for each crystalline can be calculated from Eq. (13) [25]:

$$M = \frac{\sum\limits_{j}^{5} |\gamma_j|}{d\varepsilon}, \qquad (13)$$

where γ_j is the shear strain of the particularly slip system (j) and $d\varepsilon$ is the magnitude of applied strain. The values of the obtained Taylor factors are included in Table 2.

Description of fit procedure

With the τ–γ data obtained as described in 'Simulations' section, the simulations were performed so that first the Zehetbauer's model (Eqs. 3–5) was suitably implemented into the MATLAB and Simulink toolboxes. The Levenberg–Marquardt least-square minimization method was used since it finds reliable minima even if the first guess is very far from solution, using not only a Gauss–Newton approach for parameter values close to the optimum but also the gradient descent method. The procedure systematically changes the values of C_i in search of the best fit to the experimental τ–γ data. The fitting iterations are finished when the relative changes of C_1, …, C_4 parameters are below 10^{-5}. The C_1, …, C_4 parameters are then used to calculate the evolution of the grain/cell interior size (area of screws) L_1 and the cell wall size (area of edges) L_2 using the equations (10) with support of fits of Eq. (9) to the measured dislocation densities providing the required values of α_i parameters. Also, the fractions of screw/edge areas f_1 and f_2 were optimized by iterative fitting. Table 2 lists the values of all input parameters used for the simulations.

Results and discussion

The true strain–true stress σ–ε curves of Ti–45Nb samples processed by CR&F (dashed line and squares), HPT (full line and triangles) and HE (dotted line and diamonds) are presented in Fig. 1. It is seen that until strains up to $\varepsilon = 4$ CR&F and HE processes show higher true stresses than HPT. However, the much highest true strains ($\varepsilon > 28$) are achieved by HPT. Therefore, the final hardness was larger for HPT (2.48 GPa) in comparison to the final hardness for CR&F (2.05) and to that for HE (1.81 GPa).

For the sake of simulations and using the relations of the Taylor model given in 'Simulations' section, the data presented in Fig. 1 have been recalculated to resolved shear stress τ/resolved shear strain γ ones, for direct application of the model algorithm providing the simulations. The results are shown in Fig. 2. It is seen that the τ–γ relations are—at least up to strains $\gamma = 15$—almost identical for the CR&F- and HPT-processed samples; while in case of HE-processed samples at strains beyond $\gamma > 5$, the resolved shear stress is much lower and becomes constant at much lower strains. This means that plastic deformation with CR&F and HPT processing act by different numbers and types of slip systems but essentially by the same resolved shear stress, while the deformation with HE processing follows an entirely different deformation path. This is also
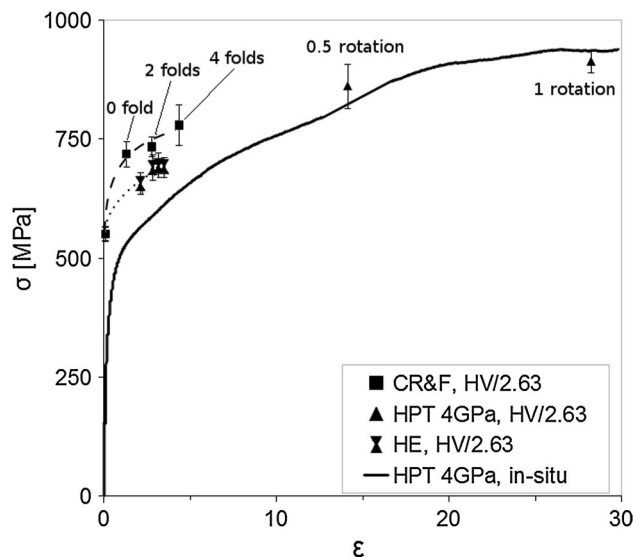

Fig. 1 True stress–true strain curves of CR&F-, HPT- and HE-processed samples. Except for the case of HPT, lines have been drawn as a guide for the eye
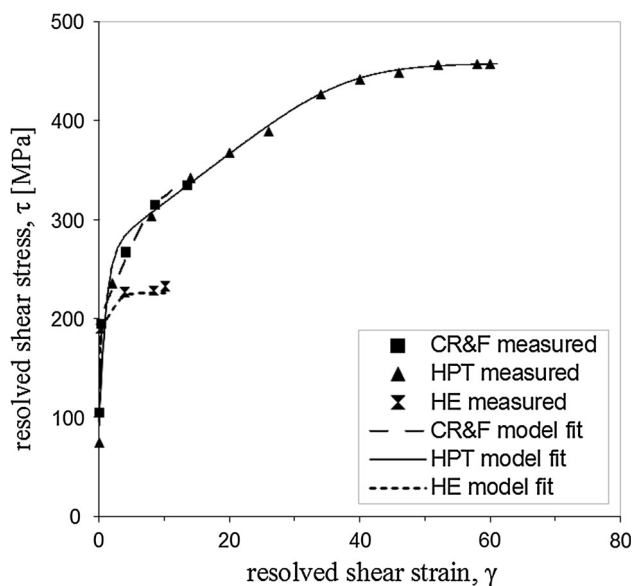
Fig. 2 The results of model simulations (*lines*) of the experimental τ–γ curves (*symbols*)
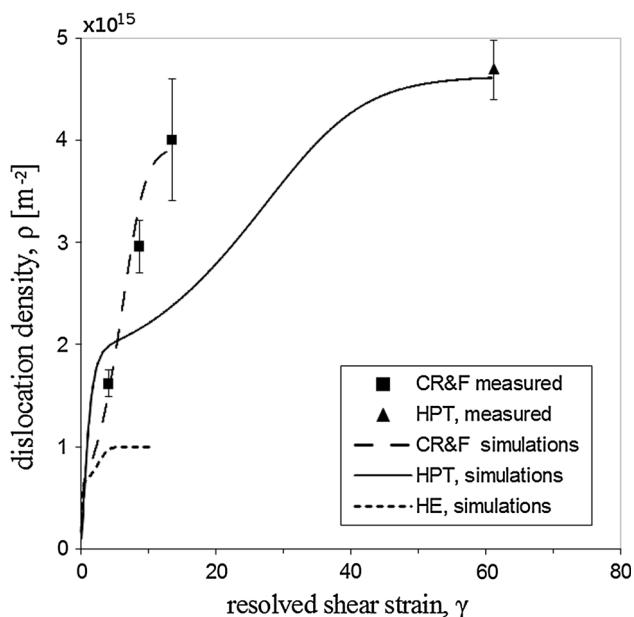

Fig. 3 Evolution of total dislocation density during CR&F, HPT and HE processes. *Full/dashed/dotted lines* result from the simulations by Zehetbauer's model. The *squares* and *triangles* represent measurements by XPA
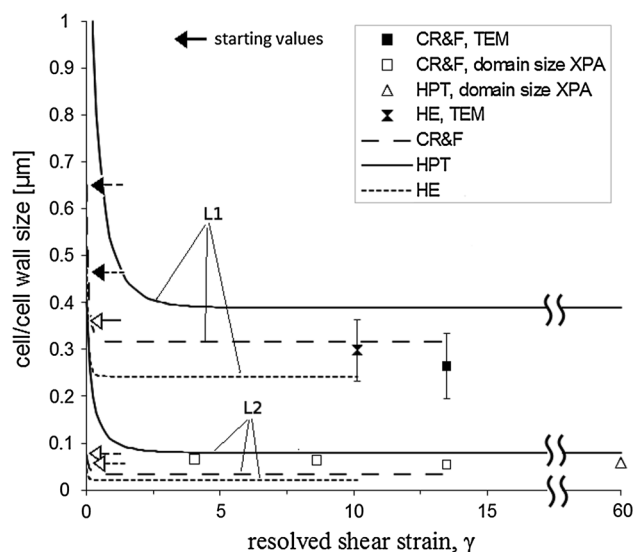

Fig. 4 Evolution of cell size (screw area L_1) and of cell wall size (edge area L_2) during CR&F and HPT processes. Full, dashed and dotted lines are from simulations by Zehetbauer's model, with arrows indicating the starting values (except L_1 for CR&F). *Open symbols* represent domain sizes measured by XPA and *full symbols* stand for grain/cell sizes derived from TEM observations. For measuring errors, see text

Table 3 Output parameters from fits of Zehetbauer's model to stress/strain characteristics of CR&F-, HPT- and HE-processed samples

Parameter/SPD method	CR&F	HPT	HE
C_1 (MPa)	663.23	219.23	1058.84
C_2 (MPa)	186.96	29.39	166.78
C_3	6.05	1.04	10.61
$C_4 \times 10^{-16}$ (MPa)	0.12	0.17	253.38
τ_0 (MPa)	98.00	92.12	95.31
β_1	10.28	25.07	6.23
β_2	42.33	291.74	48.77

indicated by the individual strain-dependent evolutions of dislocation densities (Figs. 3, 5) and of grain/cell (dislocation area) dimensions (Fig. 4) of HE processing compared to the other SPD methods.

The simulations by Zehetbauer's model have been carried out individually for each of the SPD processing routes. The fits to experimental stress–strain curves could be achieved within less than 1 % deviation. The output parameters resulting from the fit procedures for the cases of CR&F, HPT and HE processing are summarized in Table 3. The critical resolved shear stress τ_o is in the range 92–98 MPa. The β_i parameters which describe the mean free path of moving dislocations in terms of the average dislocation distance are in physically reasonable ranges, i.e. $30 > \beta_1 > 6$ and $300 > \beta_2 > 42$ (compare previous results from applications of Zehetbauer's model [15, 16, 18–21, 29]).

The results of simulations of the strain-dependent evolution of total dislocation density ρ during CR&F, HPT and HE processes are shown in Fig. 3. The final total dislocation densities amount to 4.8×10^{15} and 5.5×10^{15} m^{-2}, for CR&F- and HPT-processed samples, respectively. However, during CR&F process, the total dislocation

density beyond $\gamma = 7$ increases much faster than that during HPT. It is noticed that at a strain $\gamma \approx 10$, the total dislocation density for CR&F-processed samples is almost twice as large as that for HPT-processed samples but the resolved shear stresses are almost identical, as seen in Fig. 2. This means that a significant number of the dislocations in case of the CR&F-processed samples do not—or only little—contribute to the macroscopic stress. This point will be re-discussed below in the frame of the simulation results.

Figure 4 presents a comparison of the strain-dependent simulated parameters of nanostructure with the experimental data obtained by TEM and XPA (for details see 'Methodology' section). There is a good agreement between the simulations and experiments. The final size of grain/cell interior after fourfolds of CR&F from TEM observations is 264 ± 70 nm, while after six passes of HE the average grain/cell interior size is 298 ± 113 nm—both values being close to the edge area sizes L_1 predicted by the simulations, at least within the experimental errors. The domain size measured by XPA after fourfolds of CR&F ($\gamma \approx 13$) is 53 ± 7 nm while after one rotation of HPT ($\gamma \approx 60$) it is 56 ± 8 nm. Also, these experimental values are close to those predicted by the simulations for the edge dislocation areas L_2, as it has been found in the previous investigations of the authors [15, 16].

The simulations suggest that—as function of resolved shear strain—at first strong decreases of both the cell interior size (screw areas L_1) and cell wall size (edge areas L_2) in all the processing types occur during CR&F and HE already at much lower strains as during HPT. After that, both area sizes level out to individual constant values. Thus, the increase of strengthening above $\gamma > 3$ (Fig. 2) may not be ascribed to a Hall–Petch mechanism (from decreasing grains size) but to the considerably high dislocation density (compare Fig. 4 with Fig. 3). Such behaviour has already been observed in the other as-deformed and/or as-SPD-processed materials (HPT-processed Cu [30], Nb and Ta [31]).

However, as mentioned before, the value of the high dislocation density depends of the SPD processing method while the strengthening remains unaffected, see Fig. 3. In this situation, we can use the capability of Zehetbauer's model to analyse the evolution of dislocation density in terms of screws and edges, results of which are presented in Fig. 5 for all the SPD methods applied. It is clearly seen that the particularly strong increase of dislocations during CR&F processing is mainly due to edge dislocations which obviously do not contribute to strengthening. At the same time, however, these edge dislocations—as they are stored in the wake of and within the high-angle grain boundaries—cause an increase of misorientation angle between the adjacent grains.
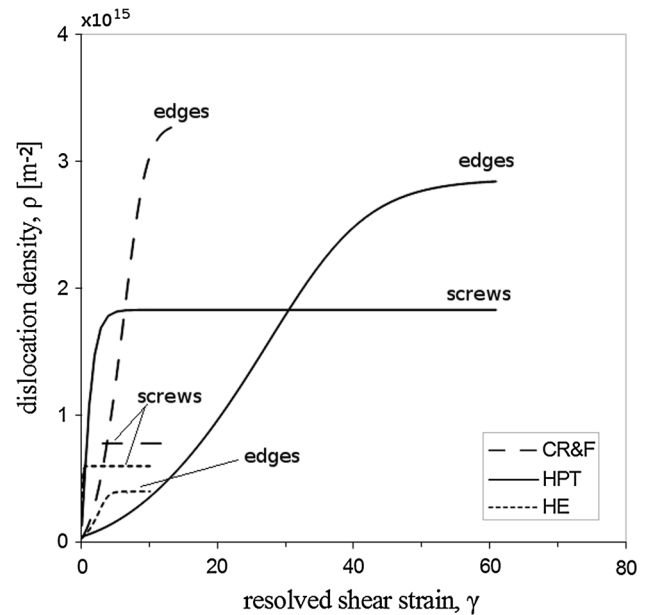

Fig. 5 Results of simulations by Zehetbauer's model on the evolution of screw and edge dislocation density during CR&F, HPT and HE processes
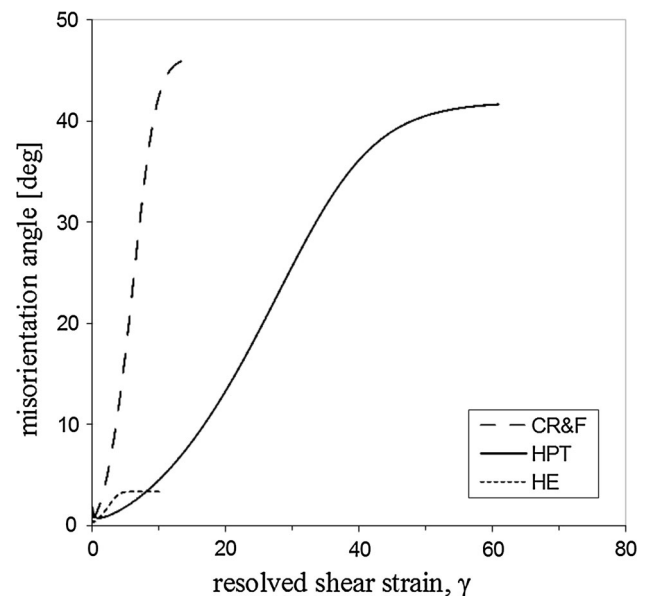

Fig. 6 Simulations of evolution of misorientation angle between adjacent grains in CR&F-, HPT- and HE-processed samples

Assuming for simplicity that all the edge dislocations in the boundary area contribute to misorientation (Eq. 11), thus allowing an estimation of an upper limit for the misorientation angle, the model can simulate the strain-dependent evolution of misorientation between the adjacent grains [16]. Applying Eq. (11) for the actual Ti–Nb SPD processings—CR&F, HPT and HE gives the graphs shown in Fig. 6. According to the rapid increase in edge
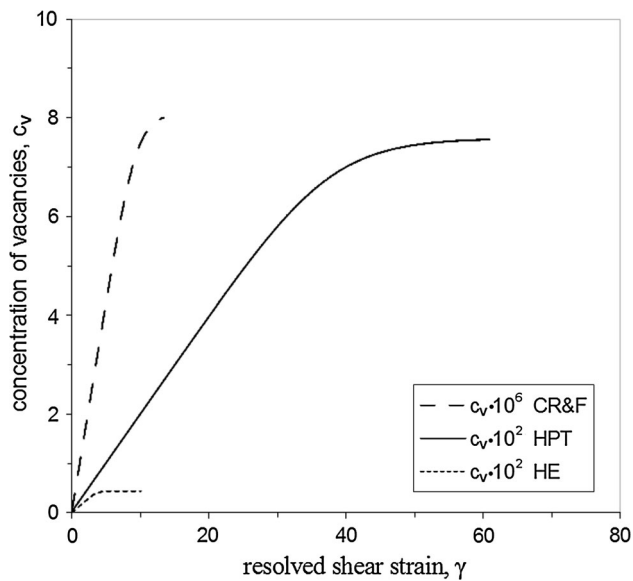
Fig. 7 Simulations of evolution of strain-induced vacancies for CR&F-, HPT- and HE-processed samples

dislocation density, the strain-dependent increase of misorientation angle of CR&F-processed samples is very fast in comparison to that of HPT- and HE-processed materials. This finding agrees with several results reported in literature [32, 33] that CR&F and/or ARB processing exhibit the most effective fragmentation and the smallest grain size among all the SPD methods. To conclude this point, it is to be noted that these dislocations described show all features of the so-called 'geometrically necessary dislocations (GNDs)' which accommodate the imposed shear strain but do not give a marked contribution to work hardening [34].

With Zehetbauer's model, it is also possible to estimate the production of SPD-induced vacancies and their concentrations as function of SPD parameters. Figure 7 presents their evolution with increasing strain for the different processing techniques CR&F, HPT and HE applied. The concentration of vacancies during HPT and HE is indicated to be up to four orders of magnitude larger in comparison to CR&F. Although this estimation again means an upper limit, it seems reasonable at least from a qualitative point of view because of the significantly high hydrostatic pressures in cases of HPT (4 GPa) and HE (1 GPa) in comparison to CR&F. Further studies—preferably detailed experimental investigations—are to be carried out in order to check those calculations.

Summary and conclusions

1. By applying SPD methods such like CR&F, HPT and HE, it is possible to significantly increase the mechanical properties of Ti–45Nb novel biomedical alloy.

2. Although the nanostructure achieved by CR&F processing is finer than that resulting from HPT, the work hardening and strength are similar. From this, it is concluded that hardening from dislocations (except from those in grain boundaries) strongly dominates that from the grain boundaries. This finding is substantiated by the fact that while at strains beyond $\varepsilon = 2.6$, no further fragmentation is indicated either in case of CR&F-, HPT- or in HE-processed samples, although work hardening is far from zero at those strains.

3. The simulations show that the fragmentation in CR&F and HE processing is stronger than that in HPT processing. In parallel, a much higher edge dislocation density in cell/grain wall area in case of CR&F is indicated suggesting a higher density of geometrically necessary dislocations than that with the other SPD methods. This is in accordance with literature findings, where the CR&F method has been described to be the most efficient one in fragmentation and minimization of grain/cell size.

4. As the simulations show good agreement with the experimental data, the large strain work-hardening model by Zehetbauer can be used to predict the evolution of strength and microstructural quantities of single-phase alloys processed by different SPD methods.

References

1. Zhao D, Chang K, Ebel T, Qian M, Willumeit R, Yanc M, Pyczak F (2013) Microstructure and mechanical behavior of metal injection molded Ti–Nb binary alloys as biomedical material. J Mech Behav Biomed Mater 28:171–182
2. Bai YJ, Wang YB, Cheng Y, Deng F, Zheng YF, Wei SC (2011) Comparative study on the corrosion behavior of Ti–Nb and TMA alloys for dental application in various artificial solutions. Mater Sci Eng, C 31:702–711
3. Banerjee R, Nag S, Stechschulte J, Fraser HL (2004) Strengthening mechanisms in Ti–Nb–Zr–Ta and Ti–Mo–Zr–Fe orthopaedic alloys. Biomaterials 25:3413–3419
4. Sumitomo N, Noritake K, Hattori T (2008) Experimental study on fracture fixation with low rigidity titanium alloy: plate fixation of tibia fracture model in rabbit. J Mater Sci 19:1581–1586. doi:10.1007/s10856-008-3372-y

5. Ozaki T, Matsumoto H, Watanabe S, Hanada S (2004) β-Ti Alloys with low Young's modulus. Mater Trans 45:2776–2779

6. Geetha M, Singh AK, Asokamani R, Gogia AK (2009) Ti-based biomaterials, the ultimate choice for orthopaedic implants—a review. Prog Mater Sci 54:397–425

7. Niinomi M (2008) Mechanical biocompatibilities of titanium alloys for biomedical applications. J Mech Behav Biomed Mater 1:30–42

8. Zehetbauer M, Zhu Y (eds) (2009) Bulk nanostructured materials. Wiley-VCH, Weinheim, Germany

9. Estrin Y, Vinogradov A (2013) Extreme grain refinement by severe plastic deformation: a wealth of challenging science. Acta Mater 61:782–817

10. Matsumoto H, Watanabe S, Hanada S (2005) β-TiNbSn alloys with low Young's modulus and high strength. Mater Trans 46:1070–1078

11. Yilmazer H, Niinomi M, Nakai M, Cho K, Hieda J, Todaka Y, Miyazaki T (2013) Mechanical properties of medical β-type Ti alloy with specific microstructural evolution through high pressure torsion. Mater Sci Eng C33:2499–2507

12. Xie KY, Wang Y, Zhao Y, Chang L, Wang G, Chen Z, Cao Y, Liao X, Lavernia EJ, Valiev RZ, Sarrafpour B, Zoellner H, Ringer SP (2013) Nanocrystalline β-Ti alloy with high hardness, low Young's modulus and excellent in vitro bio-compatibility for biomedical applications. Mater Sci Eng C33:3530–3536

13. Ozaltin K, Chrominski W, Kulczyk M, Panigrahi A, Horky J, Zehetbauer M, Lewandowska M (2014) Enhancement of mechanical properties of biocompatible Ti–45Nb alloy by hydrostatic extrusion. J Mater Sci (this issue)

14. Panigrahi A, Sulkowski B, Waitz T, Ozaltin K, Horky J, Lewandowska M, Skrotzki W, Zehetbauer M (2014) Mechanical properties and texture evolution in biocompatible Ti–45Nb alloy processed by severe plastic deformation (in press)

15. Zeipper L, Zehetbauer M, Holzleithner C (2005) Defect based micromechanical modelling and simulation of nanoSPD CP-Ti in post-deformation. Mater Sci Eng, A 410–411:217–221

16. Zehetbauer MJ, Holzleithner C, Pantleon W, Enikeev N, Sulkowski B, Spieckermann F (2014) Simulation of microstructural evolution of SPD processed nanomaterials (in press)

17. Bay B, Hansen N, Hughes DA, Kuhlmann-Wilsdorf D (1992) Evolution of f.c.c. deformation structures in polyslip. Acta Metall Mater 40:205–219

18. Zehetbauer M, Seumer V (1993) Cold work hardening in stages IV and V of F.C.C. metals—I. Experiments and interpretation. Acta Metall Mater 41:577–588

19. Zehetbauer M (1993) Cold work hardening in stages IV and V of F.C.C. metals—II. Model fits and physical results. Acta Metall Mater 41:589–599

20. Les P, Zehetbauer M (1994) Evolution of microstructural parameters in large strain deformation: description by Zehetbauer's model. Key Eng Mater 97–98:335–340

21. Zehetbauer M, Stüwe H, Vorhauer A, Schafler E, Kohout J (2003) The role of hydrostatic pressure in severe plastic deformation. Adv Eng Mater 5:330–337

22. Zehetbauer M, Schafler E, Steiner G, Korznikova E, Korznikov A (2006) Deformation induced vacancies in SPD Cu: measurements and modelling. Mater Sci Forum 503–504:57–64

23. Ungár T, Gubicza J, Ribárik G, Borbély A (2001) Crystallite size distribution and dislocation structure determined by diffraction profile analysis: principles and practical application to cubic and hexagonal crystals. J Appl Cryst 34:298–310

24. Ribárik G, Ungár T, Gubicza J (2001) MWP-fit: a program for multiple whole-profile fitting of diffraction peak profiles by ab initio theoretical functions. J Appl Cryst 34:669–676

25. Hamelin CJ, Diak BJ, Pilkey AK (2011) Multiscale modelling of the induced plastic anisotropy in bcc metals. Int J Plast 27:1185–1202

26. Tadano Y, Kuroda M, Noguchi H (2012) Quantitative re-examination of Taylor model for FCC polycrystals. Comput Mater Sci 51:290–302

27. Kraftmakher Y (1998) Equilibrium vacancies and thermophysical properties of metals. Phys Rep 299:79–188

28. Prasad S, Paul A (2012) Interdiffusion in Nb–Mo, Nb–Ti and Nb–Zr systems. Defect Diffus Forum 323–325:491–796

29. Alexandrov I, Chembarisova R, Sitdikov V, Kazyhanov V (2008) Modeling of deformation behavior of SPD nanostructured CP titanium. Mater Sci Eng, A 493:170–175

30. Dubravina A, Zehetbauer MJ, Schafler E, Alexandrov IV (2004) Correlation between domain size obtained by X-ray Bragg profile analysis and macroscopic flow stress in severely plastically deformed Cu. Mater Sci Eng, A 387–389:1018

31. Jóni B, Schafler E, Zehetbauer M, Tichy G, Ungár T (2013) Correlation between the microstructure studied by X-ray line profile analysis and the strength of high-pressure-torsion processed Nb and Ta. Acta Mater 61:632–642

32. Dinda GP, Rösner H, Wilde G (2005) Synthesis of bulk nanostructured Ni, Ti and Zr by repeated cold-rolling. Scripta Mater 52:577–582

33. Wilde G, Rösner H, Dinda GP (2005) Synthesis of nanostructures by repeated cold-rolling. Adv Eng Mater 7:11–15

34. Mughrabi H (2001) The effect of geometrically necessary dislocations on the flow stress of deformed crystals containing a heterogeneous dislocation distribution. Mater Sci Eng A319–321:139–143